

LBT Reveals Large Dust Particles and a High Mass Loss Rate for K2-22 b

EVERETT SCHLAWIN,¹ KATE Y. L. SU,¹ TERRY HERTER,² ANDREW RIDDEN-HARPER,^{2,3} AND DÁNIEL APAI^{1,4}

¹*Steward Observatory
The University of Arizona
933 North Cherry Avenue
Tucson, AZ 85721, USA*

²*Astronomy Department
Cornell University
Ithaca NY 14853*

³*Carl Sagan Institute
Cornell University
Ithaca NY 14853*

⁴*Lunar and Planetary Laboratory
The University of Arizona
1629 E. University Blvd.
Tucson, AZ 85721, USA*

ABSTRACT

The disintegrating planet candidate K2-22 b shows periodic and stochastic transits best explained by an escaping debris cloud. However, the mechanism that creates the debris cloud is unknown. The grain size of the debris as well as its sublimation rate can be helpful in understanding the environment that disintegrates the planet. Here, we present simultaneous photometry with the g band at $0.48 \mu\text{m}$ and K_S band at $2.1 \mu\text{m}$ using the Large Binocular Telescope. During an event with very low dust activity, we put a new upper limit on the size of the planet of $0.71 R_{\oplus}$ or 4500 km . We also detected a medium-depth transit which can be used to constrain the dust particle sizes. We find that the median particle size must be larger than about 0.5 to $1.0 \mu\text{m}$, depending on the composition of the debris. This leads to a high mass loss rate of about $3 \times 10^8 \text{ kg/s}$ that is consistent with hydrodynamic escape models. If they are produced by some alternate mechanism such as explosive volcanism, it would require extraordinary geological activity. Combining our upper limits on the planet size with the high mass loss rate, we find a lifetime of the planet of less than 370 Myr . This drops to just 21 Myr when adopting the $0.02 M_{\oplus}$ mass predicted from hydrodynamical models.

Keywords: stars: atmospheres — stars: individual (K2-22) — stars: variables: general

1. INTRODUCTION

The discovery of Kepler 1520 b/KIC12557548 b (Rappaport et al. 2012) ushered in a new class of extrasolar objects that are actively spewing dust off their surfaces. These disintegrating rocky objects exhibit a variety of different behaviors from periodic, e.g., Kepler-1520 b (Rappaport et al. 2012) and K2-22 b (Sanchis-Ojeda et al. 2015), to having a range of periods, e.g., WD 1145+017 (Vanderburg et al. 2015; Gary et al. 2017) to aperiodic, e.g. KIC 8462852 (Boyajian et al. 2016). The dust can cover a significant fraction of the host star and produce transit depths ranging from 0 to $\sim 60\%$ for the WD 1145+017 system (Gänsicke et al. 2016). For the K2-22 system, the transit depth range is $\sim 0\%$ to $\sim 1.3\%$ (Sanchis-Ojeda et al. 2015). The large variability and $\lesssim 0.14\%$ minimum in the transit depth indicates that the transits are dominated by dust with no significant absorption from an underlying rocky body. The dust evaporation is a stochastic process that can vary significantly from one orbit to the next. So far, there are only upper

limits on the underlying planets or asteroids producing the dusty debris. For K2-22 b, radial velocity measurements constrain the mass to $< 1.4M_J$ and shallow transit depths constrain the radius to be $< 2.5 R_\oplus$ (Sanchis-Ojeda et al. 2015).

The disintegration mechanism is not fully known, but for the systems orbiting main sequence stars like K2-22, it is hypothesized to be the hydrodynamic escape of a metal-rich planetary atmosphere that condenses into dust as it cools (Perez-Becker & Chiang 2013). Another possible mechanism could be explosive volcanism (Rappaport et al. 2012). There is an apparent correlation between starspot activity and deep transit events in the Kepler 1520 system, which suggests that high energy radiation or magnetic activity may trigger disintegration events (Kawahara et al. 2013). This is because the transit depths of Kepler 1520 b tend to be 30% deeper when the stellar flux is below average for Kepler 1520 (when the hemisphere facing Earth is covered by more spots) (Kawahara et al. 2013). However, there is an alternative suggestion that starspot occultations by the dusty debris and random groupings of starspots could create an apparent correlation (Croll et al. 2015). The 82 days of observations of K2-22 do not have the precision necessary to explore this same correlation between stellar flux and transit depths (Sanchis-Ojeda et al. 2015).

An explosive volcanic model has not been explored in detail, but Perez-Becker & Chiang (2013) calculate the mass loss history and estimate plausible masses that are compatible with hydrodynamic escape. The mass loss rate increases until it reaches a catastrophic phase toward the end of the planet’s lifetime and in this free-streaming limit the mass loss reaches a plateau. Perez-Becker & Chiang (2013) predict that there may be a population of progenitor Mercury-sized planets that are below the detection threshold of current planet searches. The hydrodynamic escape model also explains on-off behavior observed in the Kepler 1520 system where the transit depths sometimes alternate between deep and shallow transit events with each orbital period (Rappaport et al. 2012; van Werkhoven et al. 2014). This is explained by a limit cycle where the deep transit events cause shadowing and cooling of the surface and can be followed by low evaporation and shallow transit depths. These shallow transit depths expose the surface to irradiation and thus enhance atmospheric escape to produce deep transit depths later (Perez-Becker & Chiang 2013). We note that the hydrodynamic escape model is driven by visible-wavelength radiation and not X-rays or ultraviolet, so there is no requirement that stellar activity and deep transit events are correlated in the hydrodynamic escape model.

Disintegrating rocky planets provide laboratories to study the solid materials in other planetary systems. This complements studies of white dwarf atmospheric composition, where the stellar material is polluted with material from surrounding asteroids or planets (Jura 2003). So far, white dwarf atmospheric studies have revealed accurate abundances of solid material and that the accreted planetesimals largely match the bulk elemental composition of the Earth and other rocky bodies (Jura & Young 2014; Zuckerman & Young 2018). However, disintegrating bodies orbiting main sequence stars provide an avenue to studying planets before the giant stages and death of a star.

Future mid-infrared to far-infrared spectroscopic observations could yield the composition of the debris of the escaping dust. The dust debris can then be traced to either the core, mantle or crust material of a terrestrial planet. Quartz could indicate crust material, silicates could indicate mantle material, while iron can indicate core material (Bodman et al. 2018; Okuya et al. 2020a). If the planet is a coreless body (Elkins-Tanton & Seager 2008), it may also produce substantial crystalline fayalite (Fe_2SiO_4) dust (Okuya et al. 2020a). It is likely that the evaporating metal rich atmosphere around a planet will evaporate as much gas as dust in the system (Perez-Becker & Chiang 2013). So far, sodium gas has been ruled out at $\lesssim 10\%$ and ionized calcium gas at $\lesssim 2\%$ at 5σ confidence using high resolution spectroscopy (Ridden-Harper et al. 2019).

It is possible to indirectly constrain the composition of the dust debris by matching sublimation timescales with the observed tail length and particle size distribution (van Lieshout et al. 2014, 2016). Ridden-Harper et al. (2018) show that the variable transmission spectrum of Kepler 1520 b’s dust tail can be explained by varying optical depth and vertical extent. We also note that the debris’s vertical extent can also be a function of ejection speed and planet mass, so observations can constrain those related variables. In contrast to the trailing tail observed with Kepler 1520 b, K2-22 b has a leading tail, likely due to a lower ratio between radiation pressure forces and gravitational forces.

The particle size distribution can be constrained by the transmission spectrum of the debris because of the wavelength-dependence of dust extinction (Bochinski et al. 2015; Schlawin et al. 2016; Croll et al. 2014; Sanchis-Ojeda et al. 2015). Multi-band transit photometry can also be used to constrain the particle sizes of the dust escaping disintegrating planets because the dust extinction has a broad shape. Colón et al. (2018) observed K2-22 with a large ground-based campaign and find that there is no significant color dependence to the transits across $0.5 \mu\text{m}$ to $0.9 \mu\text{m}$ for high precision simultaneous coverage. Colón et al. (2018) find suggestive evidence that the g band transit depths are larger on average than the i band from stacked lightcurves but there were differences in precision and observing

windows so it is not possible to make a definitive detection of wavelength dependence other than the Gran Telescopio CANARIAS (GTC) observations of a single deep transit on February 14, 2015 (Sanchis-Ojeda et al. 2015).

Here, we obtain multi-wavelength simultaneous lightcurves using the Larger Binocular Telescope to study the debris escaping from K2-22 b. High precision multi-wavelength lightcurves can provide valuable information about K2-22 b’s particle size distribution, disintegration mechanism and indirectly provide information about composition.

LBT imaging with different filteres on the two 8.4 m mirrors is particularly suited to disintegrating planet observations because it is critical that the observations in different filters occur simultaneously. The amount of escaping debris from a disintegrating planet is highly stochastic and unpredictable from one planet orbit to the next. If observations are made in one filter on one night and a different wavelength filter a few orbits later, there is no way to distinguish the filter-dependence from temporal variability. Simultaneous lightcurves in different photometric bands, however, reveal the wavelength dependence alone.

Section 2 describes our multi-wavelength observations. We fit the lightcurves in Section 3.1. These lightcurves are used to constrain the particle size distribution in Section 3.2. We use one of the lightcurves that shows a very shallow transit depth to constrain the size of the underlying disintegration planet and its lifetime in Section 3.3. We conclude in Section 4.

2. OBSERVATIONS

We observed the K2-22 system with the Large Binocular Telescope (Rothberg et al. 2018) on three partial nights. We used the heterogenous binocular mode which allows the observatory to simultaneously point to the same target using the large binocular camera (LBC) (Giallongo et al. 2008; Speziali et al. 2008) on the SX (Left) 8.4 m mirror and the LBT Utility Camera in the Infrared 2 (LUCI2) instrument on the DX (Right) 8.4 m mirror.

We chose observing modes with the shortest and longest possible wavelengths where high signal to noise (>3000 in 10 minutes) is achievable, providing the largest change in the dust extinction function and thus the best constraints on the particle sizes. The filters satisfying this criterion are the g' band for the LBC blue instrument with a midpoint of $0.47 \mu\text{m}$ and the K_S band on the LUCI2 instrument with a midpoint of $2.16 \mu\text{m}$. We selected the K_S filter over the K -band filter to minimize the effects of telluric contamination on the observations. Imaging and spectroscopy are both possible with LUCI2, but we elected to use an imaging mode to minimize the possible sources of systematic error or slit loss.

For the LBC g' observations, we followed the modes and observing strategy of Nascimbeni et al. (2013) and Nascimbeni et al. (2015), which successfully achieved high precision observations of transiting exoplanet systems. The LUCI2 images require many calibration steps to decrease the noise in the lighcurves. All detector images must be corrected for non-linearities. For the detector non-linearity correction we use the simple (1 parameter) quadratic correction from the LBTO ¹. The flat field image calibration also required many steps, which are described in Appendix A.

The Hereford Arizona Observatory (HAO), with its 16-inch Ritchey-Chrétien telescope, was also used to monitor lightcurves of K2-22 simultaneously during two of the LBT campaigns. Given the faintness of the target, HAO photometry was obtained with an unfiltered CCD, thus integrating light from $0.4 \mu\text{m}$ to $0.85 \mu\text{m}$, making it similar to *Kepler/K2*’s bandpass but with wider wings. HAO is located at 1,400 m altitude, so telluric absorption is also

Table 1. Summary of observations

| UT start date (YYYY-mm-dd) | K Band Focus | Seeing (arcsec) | Filters | Transit Description |
|-------------------------------|--------------|--------------------|---------------|---------------------|
| 2020-01-25 | In-focus | 1.6 – 1.7 | g, K_S | Partial Transit |
| 2020-01-28 | De-focus | 1.6 – 3.5 | g, C^a, K_S | Medium |
| 2020-02-20 | In-Focus | 0.8 – 1.0 | g, K_S | Shallow |

^aOpen CCD/broadband.

¹ <https://sites.google.com/a/lbto.org/luci/instrument-characteristics/detector>

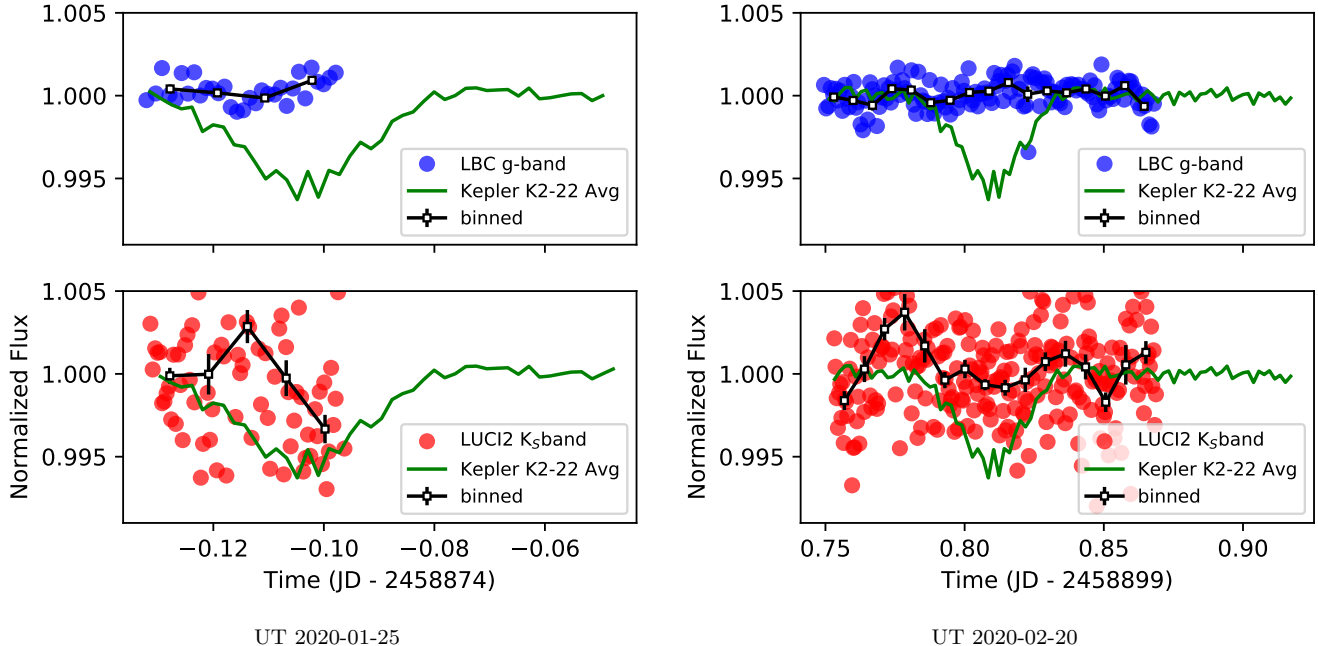


Figure 1. Photometry from UT 2020-01-25 and UT 2020-02-20 where transit depths were shallower than the K2 82 day average. The raw photometry is shown as blue and red points for the g band and K_S band, respectively, with the binned data as white squares with black error bars. The average phase-folded K2 lightcurve is shown as a green line. The photometry from UT 2020-02-20 (right) is used to constrain the size of the planet.

imprinted on the intrinsic instrument bandpass. The observing setup and reduction method is the same as [Rappaport et al. \(2016\)](#). This photometry was used as an intermediate bandpass between the g and K_S band.

A summary of the three nights of observations is listed in Table 1. To plan the observations and calculate baselines before and after transit, we use the ephemeris from ([Sanchis-Ojeda et al. 2015](#)), which has an uncertainty of 8 minutes on UT2020-01-28. Figure 1 shows photometry from UT2020-01-25. The first observation did not include enough photometry preceding the ingress of disintegrating debris to sufficiently measure the pre-ingress baseline, so this night was used as a test of the instrument mode in preparation for future observations. On UT2020-01-28, K2-22 b exhibited a moderately deep transit, as shown in Figure 2. Finally, on UT2020-02-20, K2-22 b exhibited a very shallow transit that was consistent with the out-of-transit baseline (Figure 1). This very shallow transit is used to constrain the size of the planet. For UT2020-01-28 and UT2020-02-20, we removed a linear baseline trend from the data, due either to stellar variability or a systematic drift error. The lightcurves show the time series after removing this linear trend. We bin the lightcurves to better visualize the transit depths in Figure 1 and Figure 2. The time bins are separated by 10 minutes and the errors are estimated from the standard deviation of the mean of the points within a bin.

We compare our photometry to the average level measured by the Kepler observatory, which observed K2-22 b for 82.2 days. As can be seen in Figure 2 for 2020-01-28, the K_S band transit depth was consistent with the average from the K2 mission, whereas the g band was slightly shallower. On 2020-02-20, both photometric bands exhibit shallow transit depths compared to the K2 average (see Section 3.3 for more details on this lightcurve).

The previous ephemeris has an uncertainty of 8 minutes at the time of observations. We do find that the g' and K' lightcurves for 2020-01-28 are best-fit with our model with a 7 minute shift to the data (after performing barycentric timing corrections). We do note that the lightcurve shape and timing can be variable by up to 5-10 minutes as measured by the GTC ([Colón et al. 2018](#)). Thus, we cannot robustly update the ephemeris with a single transit event. We report a tentative new ephemeris with $T_0 = 2458876.940 \pm 0.001$ BJD and $P = 0.3810771 \pm 2 \times 10^{-7}$ d, assuming that the transit shape for UT 2020-01-28 is close to the average from the K2 mission. We adopt this ephemeris for the rest of the paper for lightcurve analysis but stress that this ephemeris should be revised by an average of many transit profiles in future observational campaigns like [Colón et al. \(2018\)](#).

3. CONSTRAINTS FROM LIGHTCURVES

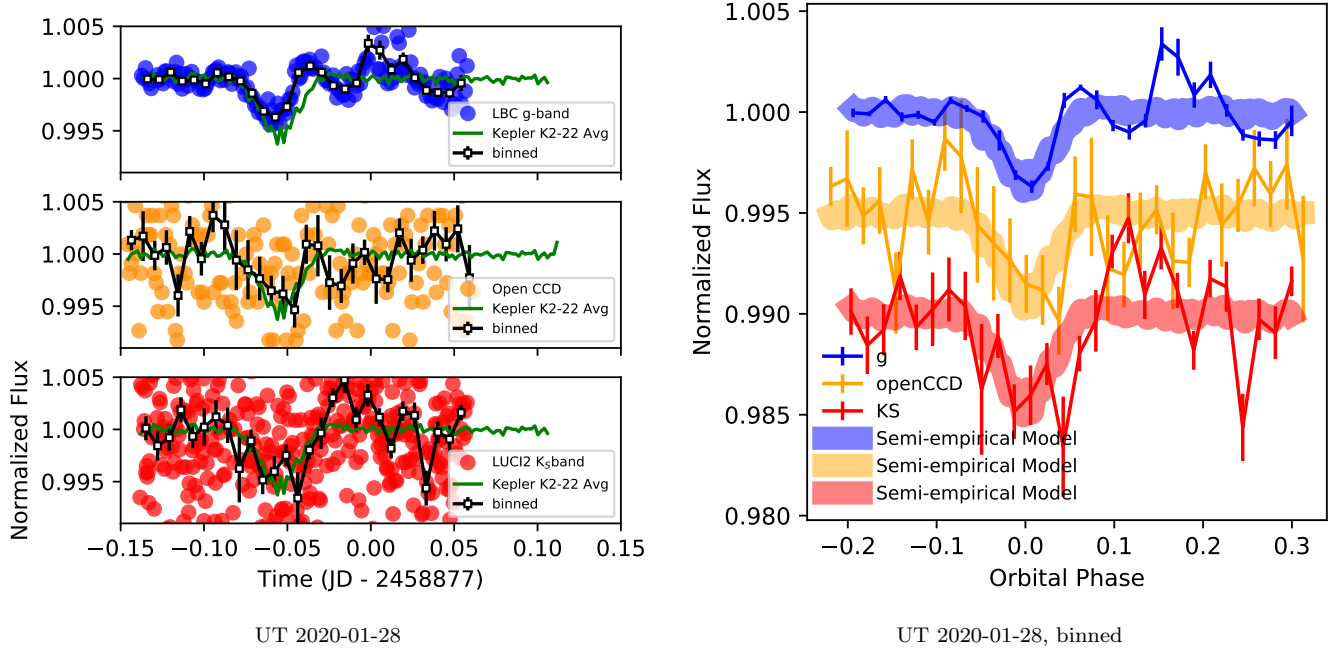


Figure 2. Photometry from UT 2020-01-28, where there was a medium-depth transit. The 82 day average lightcurve from K2 is scaled to best-fit the data, and the comparison of this scaled model with binned data is shown on the right.

The transit depths allow us to derive constraints on the particle sizes and the planet radius from the lightcurves. We first use the lightcurves where the transit depth was similar to the average from the K2 measurements to study the spectrum of the dusty debris (Section 3.1). We then model this spectrum with a dust distribution (Section 3.2). Next, we use the lightcurves where the transit depth was very shallow to constrain the planet radius (Section 3.3).

3.1. Lightcurve fitting

We used the average K2 measurements as a model to fit our measured lightcurves because the K2 lightcurves generally follow the same “V” shape. With a few higher precision ground-based GTC lightcurves (Colón et al. 2018), there are some shape variations, but we assume that the shape follows the average from the Kepler K2 measurement to reduce the number of free parameters in the tail geometry and because there can be time-correlated errors in ground-based lightcurves that can mimic shape variations. The model assumes that the dust tail leading K2-22 b varies only in optical depth (while staying optically thin with $\tau \ll 1$). We note that kinematic models of the dust ejected at ~ 1 km/s predict that the dust particles spread out to an optically thin regime when they reach a distance more than a few R_{\oplus} from the planet (van Lieshout et al. 2016). Thus, we model the lightcurve $f(\phi)$ as a function of orbital phase ϕ as

$$f(\phi) = (f_{K2}(\phi) - 1.0)a + 1.0, \quad (1)$$

where $f_{K2}(\phi)$ is the average K2 lightcurve and a is a unitless scale factor describing the transit depth. The resulting best fit lightcurves are shown in Figure 2 (right).

We use the python function `scipy.optimize.curve_fit` to fit the lightcurves. The resulting scale factors in the g band, C band and K_S bands are $a_g = 0.63 \pm 0.09$, $a_C = 0.76 \pm 0.21$ and $a_{K_S} = 0.81 \pm 0.25$, respectively. Thus, the transit depth in the K_S band is greater or equal to the g band, which indicates that the dust particles are of order-of-magnitude as large as the longer of the wavelengths ($2.16 \mu\text{m}$). In the next section, we will use a quantitative model to explore the grain size distributions in further detail.

3.2. Inferred Particle Size Distribution

We next use the transit depths that were fit in Section 3.1 to put constraints on the particle size distribution of the dusty debris escaping K2-22 b. We assume that the dust cloud is optically thin so that the transit depth scale factor

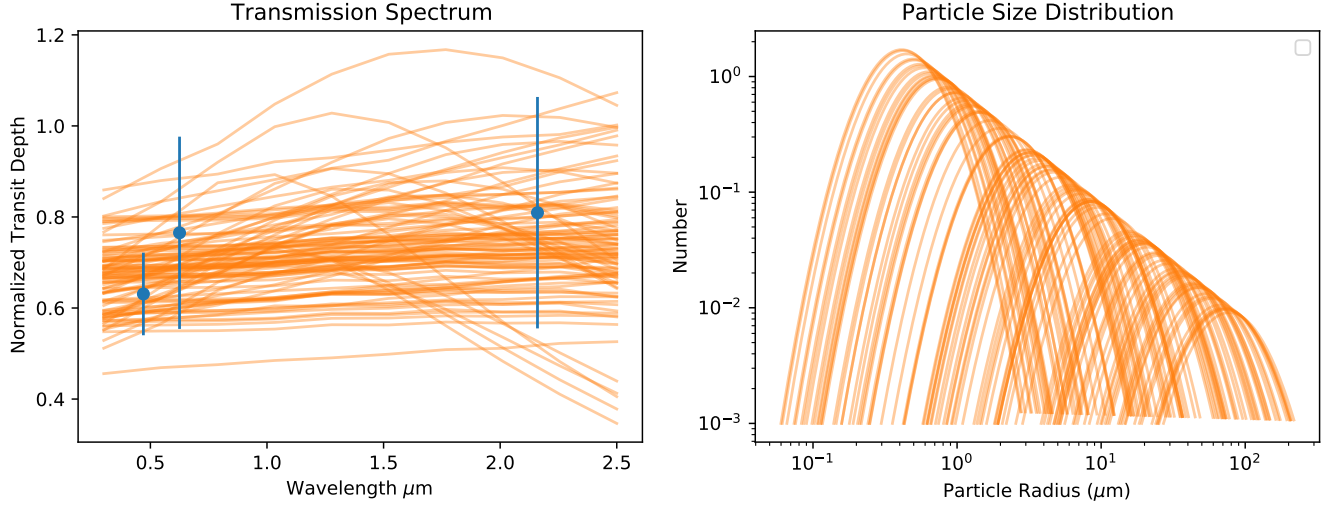


Figure 3. *Left:* Transit depths from UT 2020-01-28 (blue points with error bars) as compared to Mie extinction models for forsterite grains. Model spectra for 100 random MCMC samples are shown in orange. *Right:* Particle Size distribution for the same set of MCMC samples.

(a) is directly proportional to the average dust extinction function \bar{Q}_{ext} . Our model is then

$$a(\lambda) = A\bar{Q}_{ext}(\lambda), \quad (2)$$

where a is the transit depth scale factor from equation 1, A is a scale factor that combines the geometric coverage, particle cross section as well as the column density and $\bar{Q}_{ext}(\lambda)$ is the extinction function of the material at a given wavelength, averaged over all particles.

$$\bar{Q}_{ext}(\lambda) = \frac{\int_0^\infty n(r)Q_{ext}(\lambda, r)dr}{\int_0^\infty n(r)dr}, \quad (3)$$

where r is the particle radius and $n(r)$ is the number of particles with that radius. We start by assuming that the composition of the debris is crystalline forsterite (Mg_2SiO_4) and that the dust is composed of spherically homogeneous grains. We use the complex indices of refraction for forsterite (Suto et al. 2006) and calculate Q_{ext} using `miepython`². Later, we repeat the analysis for a suite of possible compositions.

We next use `emcee` (Foreman-Mackey et al. 2013) to derive constraints on the particle size distribution of the dusty debris escaping K2-22 b. We assume a log-normal particle size distribution so that the number of grains $n(r)$ as a function of radius r follows

$$n(r) = \frac{1}{r\sigma\sqrt{2\pi}} \exp\left(-\frac{(\ln(r) - \ln(r_{med}))^2}{2\sigma^2}\right), \quad (4)$$

where r_{med} is the median size of the grains and σ is the logarithmic width of the distribution. We fix σ at 0.5 to create a spread of particles that span several factors of r_{med} below and above the median radius. Thus, the only free parameters are r_{med} (measured in microns) and the geometric scale factor A , so the goal is to find a posterior distribution constrained by the data. A log-normal distribution is commonly used to describe atmospheric aerosols (Heintzenberg 1994) and Brownian coagulation produces aerosols with an approximately log-normal distribution (Friedlander 1977). A log-normal particle size distribution is found for amorphous pyroxene grains after vaporizing natural crystalline enstatite in a laboratory and measuring the small grain sizes (Brucato et al. 1999). We use 128 points to evaluate $n(r)$ that are spaced equally in logarithmic space and above a threshold of 10^{-3} times the total number of particles to approximate the integral in equation 3.

² <https://miepython.readthedocs.io/en/latest/>

We assume a flat prior for the logarithm of the median particle size between $\log_{10}(r_{med}) = -4$ to $\log_{10}(r_{med}) = 2$. We use 5 `emcee` walkers and run the chains for 2,000 to 3,000 steps to ensure that the chains have reached at least 50 times the autocorrelation time. The number of steps needed was different for different dust compositions. We estimate the maximum autocorrelation time for all variables with `emcee` and discard 5 times this time to remove the burn-in phase of the MCMC. Figure 3 (left) shows the spectra for 100 random samples of the posterior for r_{med} and A for forsterite composition. Figure 3 (right) shows the particle size distribution for the 100 random samples. It is clear that large particle sizes $r_{med} \gtrsim 0.5 \mu\text{m}$ are favored by the measured photometric depths.

In Figure 4, we show the posterior distribution for the median particle size of the distribution. 95% of the highest posterior density is above $0.76 \mu\text{m}$ for forsterite. We repeated this posterior distribution fit for SiO_2 (quartz), Fe (metallic iron), Fe_2SiO_4 (fayalite), MgSiO_3 (enstatite) and Al_2O_3 (corundum). Our code to evaluate the extinction coefficients is available as a Python package³. The 5% lower limit for the median dust particle size of the distribution ranges from $0.5 \mu\text{m}$ for iron to $1.0 \mu\text{m}$ for quartz. We therefore need relatively large particle sizes for K2-22 b for all compositions.

The particle sizes allow estimates of the minimum mass of the material escaping K2-22 b. We estimate the transit mass as

$$m_d \gtrsim f_{depth} R_*^2 \frac{4}{3} \pi r_{med} \rho_{dust}, \quad (5)$$

where m_d is the total mass of the dust, f_{depth} is the average transit depth, R_* is the stellar radius, r_{med} is the median particle size lower limit and ρ_{dust} is the density of dust particles (Perez-Becker & Chiang 2013). Here, we adopt the stellar radius from Sanchis-Ojeda et al. (2015) of $0.57 \pm 0.06 R_\odot$ and an average transit depth of $f_{depth} = 0.55\%$. If we assume a 0.5 to $0.9 \mu\text{m}$ particle radius for iron and quartz respectively, a density of 7.9 and 2.6 g/cm^3 (van Lieshout et al. 2016), then the total mass of the dust is $m_d \approx 1.3 \times 10^{13} \text{ kg}$ and $9.3 \times 10^{12} \text{ kg}$ for iron and quartz respectively. This assumes that the dust is optically thin with a cross section of πr_{med}^2 . The material can appear and disappear on orbital timescales so we estimate the mass loss rate as

$$\dot{M} = \frac{m_d}{P_p}, \quad (6)$$

where P_p is the period of the planet (0.381078 days, Sanchis-Ojeda et al. 2015). Thus we find $\dot{M} = 4 \times 10^8 \text{ kg/s}$ and $3 \times 10^8 \text{ kg/s}$ for iron and quartz respectively. This is 2 to 2.7 times larger than the $1.5 \times 10^8 \text{ kg/s}$ estimate in Sanchis-Ojeda et al. (2015) likely because of the larger dust size reported in this work. We note that the compositional dependence is small compared to other factors such as the particle size distribution function, optical depth and clearing timescales. We therefore adopt $3 \times 10^8 \text{ kg/s}$ as the lower limit for the characteristic \dot{M} . The true mass loss rate can be significantly higher than this value if it is optically thick or composed of particles that are much larger than $0.5 \mu\text{m}$, which is the lower limit on the median particle size estimated above. These mass loss rates only include the solid particles and the gas loss rate may be a factor of several larger considering that the gas is responsible for the hydrodynamic escape and may entrain dust particles.

We also compute \dot{M} for the Kepler 1520 system, which has similar properties. The transmission spectrum is also flat from the optical to $2.2 \mu\text{m}$ (Croll et al. 2014), giving a median particle radius $r_{med} \gtrsim 0.5 \mu\text{m}$ (Schlawin et al. 2016). The average transit depth is nearly the same as K2-22 b at 0.6% (Rappaport et al. 2012) and the radius of the star is larger at $0.69 R_\odot$ (Schlawin et al. 2018). The period is longer at 0.653 days (Rappaport et al. 2012). K2-22 b has a slightly larger estimate of \dot{M} of $3 \times 10^8 \text{ kg/s}$ versus $1.3 \times 10^8 \text{ kg/s}$ for Kepler 1520 b due to its shorter orbital period and larger median particle radius inferred from this work for a quartz composition. Altogether, the minimum mass loss rate for Kepler 1520 b and K2-22 b are consistent within the range of assumptions like spherical homogeneous grains, averages over time and optical thinness.

The mass loss rate of $3 \times 10^8 \text{ kg/s}$ for K2-22 b is consistent with a hydrodynamic escape mechanism, which produces mass loss rates $\gtrsim 10^8 \text{ kg/s}$ (Perez-Becker & Chiang 2013). Another possible escape mechanism that has been proposed is explosive volcanism (Rappaport et al. 2012). However, $3 \times 10^8 \text{ kg/s}$ is orders of magnitude higher than the most volcanically active body in our solar System, Io, which expels matter at a rate of $\sim 1000 \text{ kg/s}$ (Geissler 2003). We return to the mass loss and estimates of the planet lifetime after finding constraints on the planet size.

3.3. Planet Size Limits

³ <https://dust-mie.readthedocs.io/en/latest/>

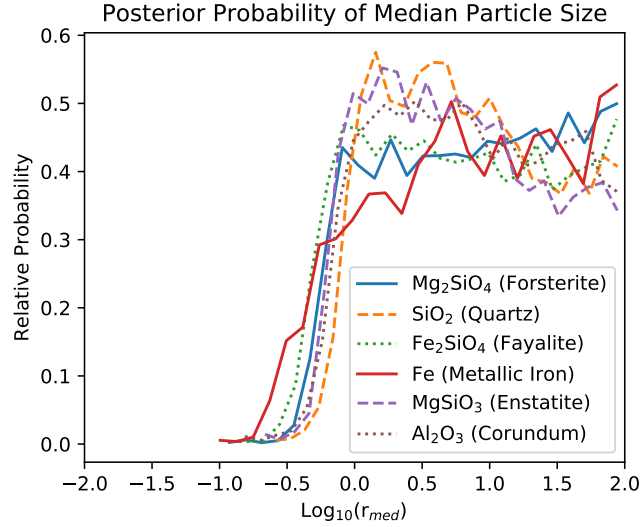


Figure 4. Posterior distribution of the median radius of the particle size distribution for different compositions. The 5% posterior lower limit of the median particle radius is $0.5 \mu\text{m}$ for iron to $0.9 \mu\text{m}$ for quartz.

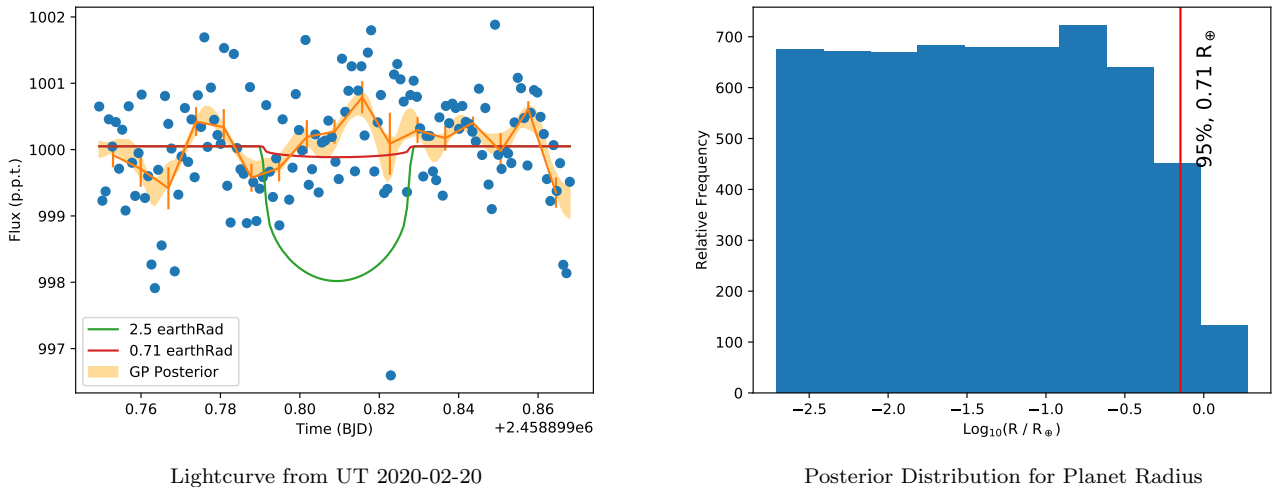


Figure 5. The g -band photometry from UT 2020-02-20 puts upper limits on the size of the underlying disintegrating planet. The minimum radius from Sanchis-Ojeda et al. (2015) of $2.5 R_{\oplus}$ is shown as a green lightcurve, as well as the 95% upper limit of $0.71 R_{\oplus}$. The lightcurve is fit with *exoplanet* (Foreman-Mackey et al. 2021) with a Gaussian process (orange 95% contours) as well as binned data for 10 minute bins (orange error bars). *Right:* Posterior distribution of the planet radius, with the 95% upper limit highlighted. The lower limit on the planet size prior comes from adding all of the observed mass loss together into a minimum size rocky planet (13 km), as discussed in Section 3.3.

The shallow transit of K2-22 b on UT 2020-02-20 allows us to put an upper limit on the size of the disintegrating planet. We note that the faintness of the system made it difficult to put accurate constraints on the size of the planet from individual transits with *K2*, with a transit depth constrained to be less than 0.14% for selected shallow transits (Sanchis-Ojeda et al. 2015). We use the g band lightcurve because it has much higher precision and smaller systematics than the K band. We fit the lightcurve using *exoplanet* (Foreman-Mackey et al. 2021) and the dependencies therein (see Software) to find the posterior distribution of the planet size.

We start by defining a prior on the planet size by estimating its minimum possible radius. K2-22 b has been disintegrating for at least the 6 years it has been observed. If we multiply a 6 year lifetime of K2-22 by \dot{M} , the minimum mass is 5×10^{16} kg. Converting this into a rocky body with a density of $5,500 \text{ kg m}^{-3}$, this value translates to a minimum radius of 13 km at the start the K2 mission. It is very unlikely that the K2 mission began observing K2-22 b just as it started to disintegrate nor that it was completely destroyed by UT 2020-02-20, so the true lifetime and radius of the planet are very likely be much larger. However, this allows us to set a prior on the planet size that is not arbitrarily small. We set a uniform prior in logarithmic space between 13 km and 10% the stellar radius (ie. $0.002 R_{\oplus}$ to $6 R_{\oplus}$). We set a pmc3 Beta function prior with $\alpha=1.0$ and $\beta=3.0$ on the impact parameter (Salvatier et al. 2016) to favor a low impact parameter because a grazing transit is both relatively unlikely by chance and would require a large vertical ejection of dust grains to produce the observed transit depths of up to $\sim 1.3\%$. We also do not detect any extremely short timescale events visible in the K2 or ground-based lightcurves as would be expected for a grazing transit. We fix the planet orbit as circular given the likely fast circularization timescales of planets at short orbital periods.

As with many ground-based lightcurves, there are time-correlated noise sources visible on all nights of observation. We model these correlations as a Gaussian process where the covariance can be modeled with a single simple harmonic oscillator term using `celerite2` (Foreman-Mackey 2018; Foreman-Mackey et al. 2017). We adopt a log-normal prior of the timescale of the correlations with a timescale of 0.02 days. We include as free parameters in the fit the mean of the lightcurve, the planet radius, the impact parameter, the Gaussian process errors and timescales. We note that the Gaussian process allows for a wider range of planet radii than a simpler lightcurve fit because it allows for the possibility that a lightcurve fluctuation could artificially lower the transit depth.

The posterior distribution of the Gaussian-process lightcurves can be seen in Figure 5. For clarity, we show the lightcurve with 10 minute long bins but the full lightcurve is used in the Gaussian process likelihood function. It is clear from the lightcurve that the upper limit of $2.5 R_{\oplus}$ from Sanchis-Ojeda et al. (2015) is improved by the LBT g-band lightcurve. The 95% upper limit in the posterior is $0.71 R_{\oplus}$ for the planet radius. This improves on the previous upper limit (Sanchis-Ojeda et al. 2015) by a factor of 3.5. K2-22 b therefore still has a range of possible radii from 13 km to 4500 km.

3.4. Planet Lifetime Limits

Combining our mass loss rate and upper size limit on the planet indicates a short lifetime for the system. If we assume it has a density of $5,500 \text{ kg m}^{-3}$, the $0.71 R_{\oplus}$ upper size limit implies a mass of 2×10^{24} kg or smaller. Combining this with the \dot{M} from above, the lifetime of the planet is less than 250 Myr. If K2-22 b is pure iron, the density could be similar to the ϵ phase of iron, or $8,300 \text{ kg m}^{-3}$ (Seager et al. 2007) and the lifetime estimate increases to 370 Myr.

The high mass loss rate observed for K2-22 b and Kepler 1520 b implies they are near the end of their lifetime. In Figure 6, we show the mass loss rate from the hydrodynamical model of Kepler 1520 b from Perez-Becker & Chiang (2013). The mass loss rate increases as the mass of the underlying planet decreases until it reaches the free streaming limit. With this model, the mass of the underlying planet is predicted to be $\lesssim 0.03 M_{\oplus}$ for an olivine composition. Putting this together with the $\dot{M} \approx 1.6 M_{\oplus}/\text{Gyr}$, the expected lifetime of the planet is $\lesssim 21$ Myr. We also use the transit depth, particle size distribution of $\gtrsim 0.5 \mu\text{m}$ from Schlawin et al. (2016) to estimate the \dot{M} for Kepler 1520 b as $1 M_{\oplus}/\text{Gyr}$ for comparison.

We use the planet lifetime calculations to estimate the occurrence rate of progenitors following Perez-Becker & Chiang (2013). We begin by estimating f_{observed} , the fraction of stars with observed disintegrating planets, using the ones from the main Kepler mission, which as a better characterized sample. There were two periodic disintegrating systems observed from the Kepler main mission: Kepler-1520 b (Rappaport et al. 2012) and KOI-2700 b (Rappaport et al. 2014). From the catalog of Berger et al. (2018), there are 116,637 FGK dwarf stars that not marked as binaries or evolved (Kunimoto & Matthews 2020). Therefore, we estimate $f_{\text{observed}} = 2/116,537$. Following Perez-Becker & Chiang (2013), we solve

$$f_{\text{observed}} \sim f_{\text{prog}} f_{\text{transit}} f_{\text{evap}}, \quad (7)$$

where f_{prog} is the occurrence rate of progenitors, f_{transit} is the geometric probability of transit ~ 0.25 and f_{evap} is the fraction of a system's lifetime where the planet is undergoing observable evaporation. The age of K2-22 is $\gtrsim 1$ Gyr (Sanchis-Ojeda et al. 2015) so we estimate f_{evap} as the 21 Myr/1 Gyr. Solving Equation 7 for f_{prog} , we find that more than $\sim 0.3\%$ of systems harbor a progenitor to a disintegrating planet. High precision future observatories may uncover new short period planets with small Mercury size or smaller bodies if they are this common.

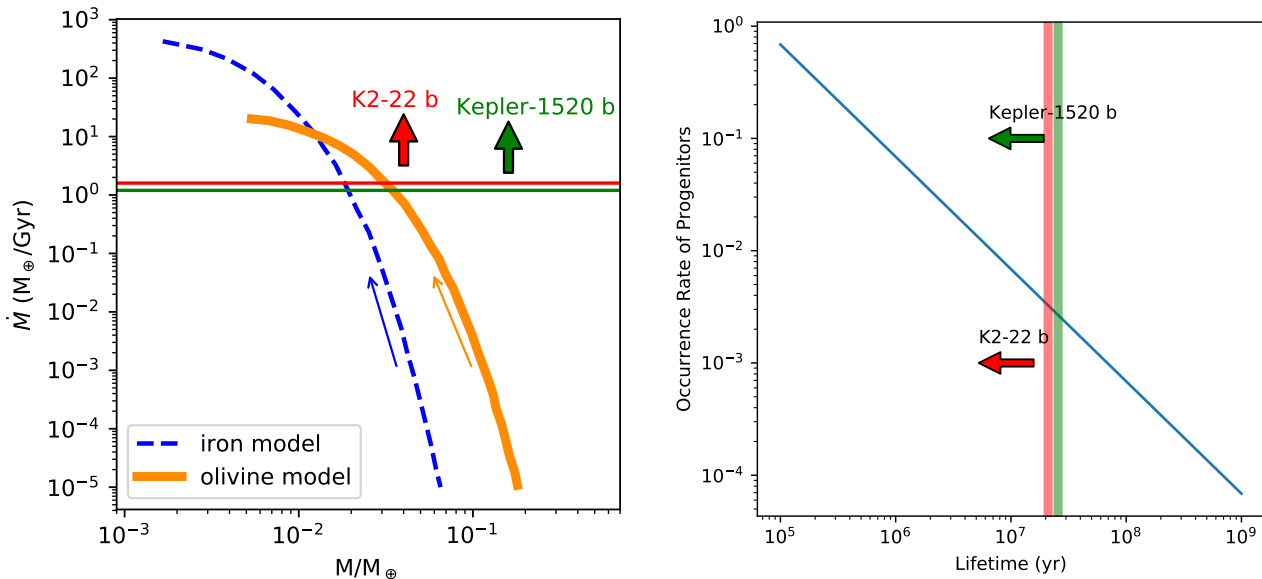


Figure 6. *Left:* The mass loss rate trajectories as a function of mass from hydrodynamical models (Perez-Becker & Chiang 2013) are indicated for an olivine composition planet and an iron composition planet in orange and blue, respectively, with arrows indicating the direction of evolution. The high mass loss rates for K2-22 b and Kepler 1520 b (with lower limits shown as horizontal red and green lines, respectively) imply that the underlying planets are in their final catastrophic state of evolution. *Right:* Given the short lifetime of the systems (with upper estimates shown as vertical lines for K2-22 b and Kepler 1520 b, respectively), we expect that short-period small progenitors may be common in more than $\sim 0.3\%$ of systems, using Equation 7.

4. CONCLUSIONS

We observed the K2-22 b system with high precision simultaneous multi-wavelength photometry with the LBT and the 16-inch Hereford observatory. We observed transits on three nights with medium to shallow transit depths as compared to the average from the K2 mission. We measured the transit depth for a medium-depth event and find that the transmission spectrum is either flat or rising slightly toward long wavelengths. This transmission spectrum allows us to constrain the dust particle size distribution. We adopt a log-normal distribution of particle sizes for a variety of single compositions. For a Mg_2SiO_4 (forsterite) composition the median particle size of the distribution is constrained to be larger than $0.8 \mu\text{m}$. This value can vary with composition from $0.5 \mu\text{m}$ for Fe (metallic iron) to $1.0 \mu\text{m}$ for SiO_2 (quartz). This is just a lower limit set by the longest wavelength ($2.16 \mu\text{m}$), so the median particle size could be larger for all compositions. Observations with JWST NIRSpec and MIRI can place valuable new constraints on the particle size distribution as well as the composition through mid-infrared solid state features (Bodman et al. 2018; Okuya et al. 2020b).

The large particle sizes, larger surface area and the short time for the dust tail to be cleared and recreated (1 orbital period or 0.4 days) implies a large mass loss rate for the planet of $\dot{M} \gtrsim 3 \times 10^8 \text{ kg/s}$ or equivalently $1.6 M_{\oplus}/\text{Gyr}$. This is just a lower limit for the mass loss rate because the particles could be significantly larger than $0.5 \mu\text{m}$. Hydrodynamic escape of a metal-rich atmosphere surrounding the planet (Perez-Becker & Chiang 2013) predicts that 10^8 kg/s mass loss rates are possible in a planet’s final catastrophic phase of disintegration. One other mechanism that has been discussed is explosive volcanism (Rappaport et al. 2012). We note that the observed minimum \dot{M} is orders of magnitude higher than has been observed for dusty mass loss in the present-day Solar System ($\dot{M}_{Io} \approx 1000 \text{ kg/s}$ Geissler 2003), so it would require much more vigorous activity for K2-22 b’s mass loss to be produced by volcanism.

We also used the very shallow transit depth of UT 2020-02-20 to put new upper limits on the size of the underlying disintegrating planet. We used the mass loss rate and the fact that disintegration has been observed for at least 6

years to set the minimum radius prior. Our upper limit is $0.71 R_{\oplus}$ compared to the previous value of $2.5 R_{\oplus}$. The range of allowed radii is 13 km to 4500 km.

Combining the \dot{M} with our radius constraints, the characteristic lifetime of the planet (M/\dot{M}) is $\lesssim 370$ Myr. It is $\lesssim 21$ Myr when assuming the mass from a hydrodynamic model (Perez-Becker & Chiang 2013). This relatively short lifetime indicates we are observing a short catastrophic phase of the planet disintegration. If K2-22 b and another disintegrating planet Kepler 1520 b have lifetimes this short, it implies that their progenitors are common. We expect that high precision results from future transit surveys may uncover that short period Mercury and smaller-size progenitors occur in more than $\sim 0.3\%$ of systems.

ACKNOWLEDGEMENTS

Funding for E Schlawin is provided by NASA Goddard Spaceflight Center. This research has made use of NASA's Astrophysics Data System Bibliographic Services. We are very grateful to Bruce Gary for providing lead-up photometry as well as the simultaneous unfiltered CCD photometry and his feedback on this work. We wish to thank Olga Kuhn, Jennifer Power, Andrew Cardwell and Michelle Edwards for invaluable work preparing and observing in the LBT mixed-mode time series. We acknowledge support from the Earths in Other Solar Systems Project (EOS, PI: Apai), grant No. 3013511 sponsored by NASA. The results reported herein benefited from collaborations and/or information exchange within NASA's Nexus for Exoplanet System Science (NExSS) research coordination network sponsored by NASA's Science Mission Directorate. Thank you to Graham Lee and Jake Taylor for compiling and sharing the complex indexes of refraction for the dust particles used in this work. We thank the anonymous reviewer for taking the time to review this work and provide helpful clarifications and corrections.

Facilities: Kepler, LBT(LBCB and LUCI2)

Software: `astropy` (Astropy Collaboration et al. 2013), `emcee` (Foreman-Mackey et al. 2013), `photutils v0.3` (Bradley et al. 2016), `ccdproc` (Craig et al. 2015) `matplotlib` (Hunter 2007), `numpy` (van der Walt et al. 2011), `scipy` (Virtanen et al. 2020), `pymc3`, (Salvatier et al. 2016), `starry` (Luger et al. 2019), `arviz`, (Kumar et al. 2019), `theano`, (Theano Development Team 2016), `exoplanet` (Foreman-Mackey et al. 2021; Agolet et al. 2020), `celerite` (Foreman-Mackey 2018; Foreman-Mackey et al. 2017)

APPENDIX

A. FLAT FIELD CALIBRATION IMAGE CREATION

The dome flat field was observed at high and low lamp illumination, so we made average flat fields of all exposures (f_{high} and f_{low}) for the high and low illumination levels. We expected to subtracted the two values, ie.

$$f_{original} = \frac{f_{high} - f_{low}}{Med(f_{high} - f_{low})}, \quad (A1)$$

where $Med()$ is the median of an image to normalize it to 1.0. However, it was necessary to add a further correction proportional to the ratio of the high and low illumination flat field. We used the following prescription for the flat field:

$$f_{final} = (f_{high} - f_{low}) \times (-2.0(f_{ratio} - 1.0) + 1.0), \quad (A2)$$

where

$$f_{ratio} = \frac{f_{high}/f_{low}}{Med(f_{high}/f_{low})}. \quad (A3)$$

As shown in Figure 7, applying the modified flat field has less pronounced horizontal stripes than the unmodified original flat field. This reduces the position-dependence of the time series.

After the flat field correction, there are many bad pixels in f_{ratio} near the target and reference stars that can affect photometry. We identified the bad pixels from f_{ratio} : any points below 0.93 or 1.25 from the median were marked as bad pixels. Values this far from the median ratio indicated that the pixels responded highly non-linearly or not at all with respect to the median pixel response. Also, any points with $f_{high} - f_{low} < 1600$ counts were marked as bad pixels

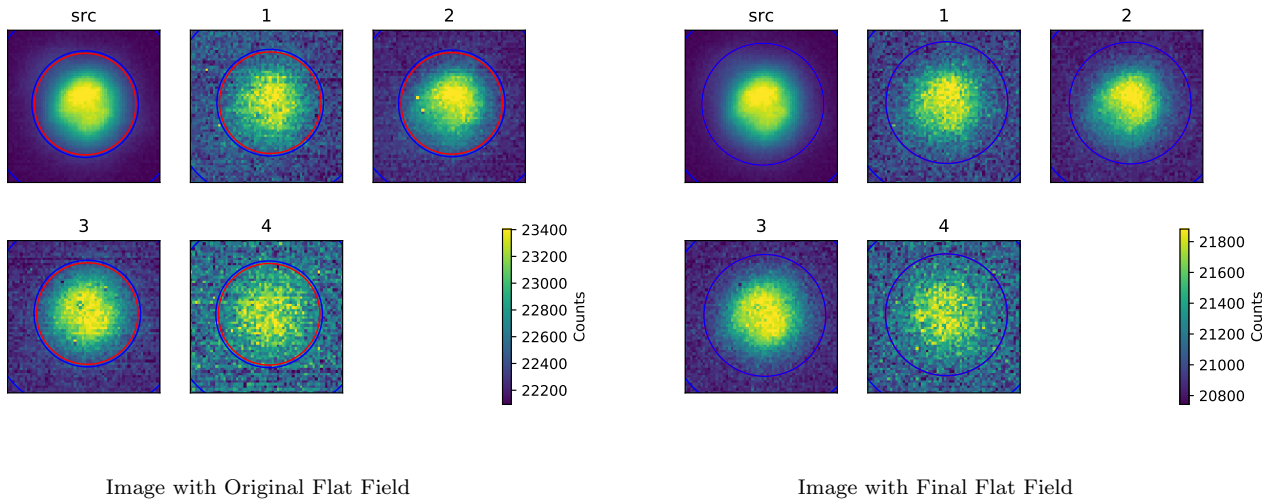


Figure 7. Postage stamp cutouts near the K2-22 and reference stars used to remove common-mode systematics for the infrared LUCI2 HgCdTe detector. Applying the modified flat field from Equation A2 reduces the horizontal striping (most visible in star 4) in the science images. Additionally, replacing the bad pixels in the flat field calibration image reduces the number of artifacts in the science data.

because they did not respond to the differential flux. The bad pixels in f_{ratio} are replaced with 1.0. The resulting flat field produces fewer bad pixels in the final reduced images, as seen in Figure 7.

REFERENCES

- Agol, E., Luger, R., & Foreman-Mackey, D. 2020, *AJ*, 159, 123 [ADS]
- Astropy Collaboration, Robitaille, T. P., Tollerud, E. J., et al. 2013, *A&A*, 558, A33 [ADS]
- Berger, T. A., Huber, D., Gaidos, E., & van Saders, J. L. 2018, *ApJ*, 866, 99 [ADS]
- Bochinski, J. J., Haswell, C. A., Marsh, T. R., Dhillon, V. S., & Littlefair, S. P. 2015, *ApJL*, 800, L21 [ADS]
- Bodman, E. H. L., Wright, J. T., Desch, S. J., & Lisse, C. M. 2018, *AJ*, 156, 173 [ADS]
- Boyajian, T. S., LaCourse, D. M., Rappaport, S. A., et al. 2016, *MNRAS*, 457, 3988 [ADS]
- Bradley, L., Sipocz, B., Robitaille, T., et al. 2016, *astropy/photutils: v0.3*, doi:10.5281/zenodo.164986 [LINK]
- Brucato, J. R., Colangeli, L., Mennella, V., Palumbo, P., & Bussoletti, E. 1999, *A&A*, 348, 1012 [ADS]
- Colón, K. D., Zhou, G., Shporer, A., et al. 2018, *AJ*, 156, 227 [ADS]
- Craig, M. W., Crawford, S. M., Deil, C., et al. 2015, *ccdproc: CCD data reduction software, Astrophysics Source Code Library*, ascl:1510.007 [ADS]
- Croll, B., Rappaport, S., & Levine, A. M. 2015, *MNRAS*, 449, 1408 [ADS]
- Croll, B., Rappaport, S., DeVore, J., et al. 2014, *ApJ*, 786, 100 [ADS]
- Elkins-Tanton, L. T., & Seager, S. 2008, *ApJ*, 688, 628 [ADS]
- Foreman-Mackey, D. 2018, *Research Notes of the American Astronomical Society*, 2, 31 [ADS]
- Foreman-Mackey, D., Agol, E., Ambikasaran, S., & Angus, R. 2017, *AJ*, 154, 220 [ADS]
- Foreman-Mackey, D., Hogg, D. W., Lang, D., & Goodman, J. 2013, *PASP*, 125, 306 [ADS]
- Foreman-Mackey, D., Savel, A., Luger, R., et al. 2021, *exoplanet-dev/exoplanet v0.4.4*, doi:10.5281/zenodo.1998447
- Friedlander, S. K. 1977, *Smoke, dust and haze: Fundamentals of aerosol behavior* (Oxford University Press) [ADS]
- Gänsicke, B. T., Aungwerojwit, A., Marsh, T. R., et al. 2016, *ApJL*, 818, L7 [ADS]
- Gary, B. L., Rappaport, S., Kaye, T. G., Alonso, R., & Hamschs, F.-J. 2017, *MNRAS*, 465, 3267 [ADS]
- Geissler, P. E. 2003, *Annual Review of Earth and Planetary Sciences*, 31, 175 [ADS]
- Gjallongo, E., Ragazzoni, R., Grazian, A., et al. 2008, *A&A*, 482, 349 [ADS]

- Hayakawa, Y. S., & Matsukura, Y. 2009, *Geomorphology*, 110, 212 [ADS]
- Heintzenberg, J. 1994, *Aerosol Science Technology*, 21, 46 [ADS]
- Hunter, J. D. 2007, *Computing In Science & Engineering*, 9, 90
- Jura, M. 2003, *ApJL*, 584, L91 [ADS]
- Jura, M., & Young, E. D. 2014, *Annual Review of Earth and Planetary Sciences*, 42, 45 [ADS]
- Kawahara, H., Hirano, T., Kurosaki, K., Ito, Y., & Ikoma, M. 2013, *ApJL*, 776, L6 [ADS]
- Kumar, R., Carroll, C., Hartikainen, A., & Martin, O. A. 2019, *The Journal of Open Source Software*, doi:10.21105/joss.01143
- Kunimoto, M., & Matthews, J. M. 2020, *AJ*, 159, 248 [ADS]
- Luger, R., Agol, E., Foreman-Mackey, D., et al. 2019, *AJ*, 157, 64 [ADS]
- Nascimbeni, V., Piotto, G., Pagano, I., et al. 2013, *A&A*, 559, A32 [ADS]
- Nascimbeni, V., Mallonn, M., Scandariato, G., et al. 2015, *A&A*, 579, A113 [ADS]
- Okuya, A., Okuzumi, S., Ohno, K., & Hirano, T. 2020a, arXiv e-prints, arXiv:2008.07781 [ADS]
- . 2020b, *ApJ*, 901, 171 [ADS]
- Perez-Becker, D., & Chiang, E. 2013, *MNRAS*, 433, 2294 [ADS]
- Rampino, M. R., & Self, S. 1982, *Quaternary Research*, 18, 127 [ADS]
- Rappaport, S., Barclay, T., DeVore, J., et al. 2014, *ApJ*, 784, 40 [ADS]
- Rappaport, S., Gary, B. L., Kaye, T., et al. 2016, *MNRAS*, 458, 3904 [ADS]
- Rappaport, S., Levine, A., Chiang, E., et al. 2012, *ApJ*, 752, 1 [ADS]
- Ridden-Harper, A. R., Keller, C. U., Min, M., van Lieshout, R., & Snellen, I. A. G. 2018, *A&A*, 618, A97 [ADS]
- Ridden-Harper, A. R., Snellen, I. A. G., Keller, C. U., & Mollière, P. 2019, *A&A*, 628, A70 [ADS]
- Rothberg, B., Kuhn, O., Power, J., et al. 2018, in *Society of Photo-Optical Instrumentation Engineers (SPIE) Conference Series*, Vol. 10702, *Ground-based and Airborne Instrumentation for Astronomy VII*, ed. C. J. Evans, L. Simard, & H. Takami, 1070205 [ADS]
- Salvatier, J., Wiecki, T. V., & Fonnesbeck, C. 2016, *PeerJ Computer Science*, 2, e55
- Sanchis-Ojeda, R., Rappaport, S., Pallè, E., et al. 2015, *ApJ*, 812, 112 [ADS]
- Schlawin, E., Herter, T., Zhao, M., Teske, J. K., & Chen, H. 2016, *ApJ*, 826, 156 [ADS]
- Schlawin, E., Hirano, T., Kawahara, H., et al. 2018, *AJ*, 156, 281 [ADS]
- Seager, S., Kuchner, M., Hier-Majumder, C. A., & Militzer, B. 2007, *ApJ*, 669, 1279 [ADS]
- Speziali, R., Di Paola, A., Giallongo, E., et al. 2008, in *Society of Photo-Optical Instrumentation Engineers (SPIE) Conference Series*, Vol. 7014, *Ground-based and Airborne Instrumentation for Astronomy II*, ed. I. S. McLean & M. M. Casali, 70144T [ADS]
- Suto, H., Koike, C., Chihara, H., Sogawa, H., & Tachibana, S. 2006, *Astronomical Herald*, 99, 682 [ADS]
- Theano Development Team. 2016, arXiv e-prints, abs/1605.02688
- van der Walt, S., Colbert, S. C., & Varoquaux, G. 2011, *Computing in Science and Engineering*, 13, 22 [ADS]
- van Lieshout, R., Min, M., & Dominik, C. 2014, *A&A*, 572, A76 [ADS]
- van Lieshout, R., Min, M., Dominik, C., et al. 2016, *A&A*, 596, A32 [ADS]
- van Werkhoven, T. I. M., Brogi, M., Snellen, I. A. G., & Keller, C. U. 2014, *A&A*, 561, A3 [ADS]
- Vanderburg, A., Johnson, J. A., Rappaport, S., et al. 2015, *Nature*, 526, 546 [ADS]
- Virtanen, P., Gommers, R., Oliphant, T. E., et al. 2020, *Nature Methods*, 17, 261 [LINK]
- Zuckerman, B., & Young, E. D. 2018, *Characterizing the Chemistry of Planetary Materials Around White Dwarf Stars* (Springer), 14 [ADS]